The Causal Relation within Air–Sea Interaction as Inferred from Observations

YANG YANG,[a] RUI XIN HUANG,[b] X. SAN LIANG,[c,d] ZHIYU LIU,[a] JIANYU HU,[a] YUHUI ZHAO,[e] AND GUANQI FU[a]

[a] *State Key Laboratory of Marine Environmental Science, and Department of Physical Oceanography, College of Ocean and Earth Sciences, Xiamen University, Xiamen, China*
[b] *Department of Physical Oceanography, Woods Hole Oceanographic Institution, Woods Hole, Massachusetts*
[c] *The Artificial Intelligence Department, Division of Frontier Research, Southern Marine Science and Engineering Guangdong Laboratory (Zhuhai), Zhuhai, China*
[d] *Department of Atmospheric and Oceanic Sciences, Institute of Atmospheric Sciences, Fudan University, Shanghai, China*
[e] *School of Marine Sciences, Nanjing University of Information Science and Technology, Nanjing, China*

(Manuscript received 14 December 2023, in final form 3 September 2024, accepted 4 October 2024)

ABSTRACT: The intricate cause–effect relations in air–sea interaction are investigated using a quantitative causal inference formalism. The formalism is first validated with a classical stochastic coupled model and then applied to the observational time series of sea surface temperature (SST) and air–sea turbulent surface heat flux (SHF). We identify an overall asymmetry of causality between the two variables, namely, the causality from SHF to SST is significantly larger than that from SST to SHF over most of the global oceans. Geographically, the coupling is strongest in the tropics and gets weaker substantially in the extratropics. In the midlatitude ocean, SST makes higher contributions to the SHF variability in frontal regions. We further show that the identified causality is space and time scale dependent. The dominance of SHF driving SST occurs at basin scales, whereas the dominance of SST driving SHF mostly occurs at scales smaller than 10°. The causalities in both directions get larger with increasing time scale and are less asymmetric at longer time scales. The seasonality of the causality is also discussed here.

KEYWORDS: Atmosphere-ocean interaction; Sea surface temperature; Air-sea interaction; Surface fluxes; Stochastic models

1. Introduction

The ocean and atmosphere interact by exchanging heat, momentum, and freshwater at the air–sea interface. These interactions play an important role in regulating the Earth system, influencing regional and global climate (e.g., Wallace et al. 1990; Bladé 1997; Barsugli and Battisti 1998).

Fundamental questions studied in this field for decades concern the coupled relationships between the two systems (e.g., Frankignoul 1985; Kalnay et al. 1986; Small et al. 2008; Chelton and Xie 2010; Seo et al. 2023). Early studies using stochastic models suggest that the sea surface temperature (SST) variability in the extratropics is primarily generated by atmospheric forcing (Hasselmann 1976; Frankignoul and Hasselmann 1977). These models successfully capture an important feature of Earth's climate over much of the extratropical ocean, that is, the reddening of the SST spectrum responding to synoptic "white noise" atmospheric forcing. However, this classical atmosphere-driving paradigm has later been shown not to hold in many places, such as the western boundary current (WBC) and the Antarctic Circumpolar Current (ACC) regions, where sharp SST gradients exist. In these regions, the SST anomalies associated with fronts and eddies induce surface turbulent heat and momentum flux anomalies that exert significant influences on the atmospheric boundary layer (e.g., Chelton et al. 2004; Small et al. 2008). The forced atmosphere in turn invokes various feedback processes that could further imprint on the ocean. Numerical studies have shown evidence that the two-way coupling tends to damp the oceanic eddy available potential energy and eddy kinetic energy, mainly through thermal feedbacks (e.g., Ma et al. 2016; Bishop et al. 2020) and current feedbacks (e.g., Duhaut and Straub 2006; Renault et al. 2016), respectively.

To identify the regime of air–sea interaction from time series, a common practice in literature is to conduct lead–lag correlation analyses between SST and interfacial variables (i.e., surface turbulent heat fluxes and wind stress) or near-surface meteorological variables (wind, air temperature, sea surface pressure, and low-level vorticity). Among these, the statistical relationship between local SST and turbulent surface heat flux (SHF) is of particular interest. In seminal works by Hasselmann (1976) and Frankignoul and Hasselmann (1977), an idealized stochastic model was developed for the SST–SHF covariability. Continuing efforts since then have been made to extend the model and improve our understanding of the air–sea interaction. Research along this line includes Cayan (1992), Barsugli and Battisti (1998), Frankignoul et al. (1998), von Storch (2000), Wu et al. (2006), Kirtman et al. (2012), Li et al. (2017), Bishop et al. (2017), Small et al. (2019), and Patrizio and Thompson (2022), to name a few.

As summarized in Bishop et al. (2017) and Small et al. (2019), when a significant amount of atmospheric "noise" (i.e., the weather system) is presented in the coupled model, the correlation between SST and SHF is antisymmetric about zero lag, with near-zero simultaneous correlation. Correspondingly, the correlation between SST tendency and SHF is symmetric, with large negative simultaneous correlation. Note that in this paper, a positive SHF means heat releases from the ocean to the atmosphere and it is associated with a cooling of

---

Corresponding author: Yang Yang, yyang2@xmu.edu.cn

DOI: 10.1175/JCLI-D-23-0742.1

the ocean; thus, the above scenario indicates that the atmosphere forces the ocean. Such kind of SST–SHF relationship has been found in the extratropical ocean at regions away from strong current systems (e.g., Cayan 1992; von Storch 2000; Bishop et al. 2017). Conversely, when the oceanic noise (i.e., the mesoscale eddies and fronts) is present, there is a strong positive simultaneous correlation between SST and SHF, whereas the correlation between SST tendency and SHF is antisymmetric about zero lag, with a positive correlation when SST tendency leads SHF. This scenario can be regarded as one where the ocean forces the atmosphere (i.e., warm ocean heats the atmosphere and vice versa), and the SHF functions to damp the SST anomalies generated by interior oceanic processes. A large number of recent studies have reported positive SST–SHF correlation over ocean sectors where frontal variability is most energetic (e.g., Bishop et al. 2017; Small et al. 2019).

While the results of the abovementioned studies have greatly improved our understanding of the air–sea interaction and its associated regional- and scale-dependent characteristics, the so-obtained empirical rules rely on correlation analysis, which is not sufficient to imply causality. More importantly, as pointed out by Sutton and Mathieu (2002) and many others, the intricate interactions and feedbacks embedded in the coupled atmosphere–ocean system pose great challenges on identification of the underlying causalities among mutually interacting variables. In this paper, we go beyond previous approaches by using an information flow (IF)-based causal inference approach to quantify the local air–sea interaction. This method is quantitative in nature and gives an easy-to-use formula only involving a combination of some sample covariances. For the sake of simplicity and comparison with the results shown in previous studies (e.g., Barsugli and Battisti 1998; von Storch 2000; Wu et al. 2006; Bishop et al. 2017; Small et al. 2019; Docquier et al. 2023), we will only focus on the local SST–SHF coupling in this study.

It is worth mentioning that a recent paper by Docquier et al. (2023) addressed the SST–SHF causality using the same method of IF as in this study. In their study, the authors used monthly averaged data so that their focus was at the monthly time scale. The present study, however, uses daily averaged data considering that the atmospheric "weather noise" essentially lies on the synoptic time scale (a few days). Monthly averaging filters out the atmospheric forcing of SST on these short time scales. The present study further extends the analysis into the temporal- and spatial-scale dependences as well as their seasonality, aiming to add further knowledge to the field of local air–sea interaction.

The rest of the paper is organized in the following logical order. In section 2, we describe the causal inference method and the satellite-based data. In section 3, a well-known idealized stochastic coupling model is used to verify the performance of the causal inference method. In section 4, we apply the method to observational data, with an aim to map out the causality between SST and SHF globally, and understand its regionality, seasonality, and scale-dependent characteristics. This study is summarized in section 5.

2. Methods and data

a. *Quantitative causality analysis*

In information theory, causality is identified by IF. That is, if a source variable causes variation in a destination variable, information would flow (transfer) from the source variable to the destination variable (e.g., Lloyd 1991). Shannon (1948) first introduced the concept of entropy as a measure of information content or uncertainty of an event. Generally, a more certain event contains less information. Recently, Liang (2016) formulated the IF within the framework of the dynamical system [This line of work includes a series of published papers by Liang (2008, 2014, 2015, 2016, 2021).] Rather than axiomatically proposed, Liang's formula is derived analytically. In his formalism, the IF, and thus causality from process x_2 to another process x_1, is defined as the contribution of entropy from x_2 per unit time to the entropy change of x_1. It satisfies the principle of nil causality, which states that if the variation of x_1 does not depend on x_2, then the IF from x_2 to x_1 should be zero. This seemingly obvious fact, however, needs to be tested in applications in all previous formalisms. In contrast, here, it appears as a proven theorem. In the following, we present a concise introduction to this method. The complete derivation is rather lengthy; readers are referred to Liang (2016) and related papers listed above for details.

In the context of a dynamical system with its dynamics analytically described, Liang (2014) obtained a rigorous formula for IF, which is based on infinitely many realizations generated by the known dynamical system. In real-world applications, a problem naturally arises: how the IF can be quantified without knowing the dynamical system but only given times series (i.e., one realization of each variable)? In this case, Liang (2014) showed that, in the linear limit, the IF can be estimated from time series through maximum likelihood estimation (MLE). Given two time series x_1 and x_2, the MLE of IF from x_2 to x_1 is

$$T_{2\to 1} = \frac{C_{11}C_{12}C_{2,d1} - C_{12}^2 C_{1,d1}}{C_{11}^2 C_{22} - C_{11}C_{12}^2}, \qquad (1)$$

where C_{ij} is the sample covariance between x_i and x_j, $C_{i,dj}$ is the covariance between x_i and $\dot{x}_j$, and $\dot{x}_j$ denotes the difference approximation of dx_j/dt. The MLE of the IF in the opposite direction can be directly written out by switching the indices.

Although under a linear assumption, Eq. (1) has been validated in highly nonlinear system problems (Liang 2014). So far, this method has been validated and applied with success in many disciplines, such as atmosphere–ocean science, data science, neuroscience, and quantum mechanics (e.g., Stips et al. 2016; Hristopulos et al. 2019; Liang et al. 2021; Yang et al. 2023; Yi and Bose 2022; Liang et al. 2023).

Note that Eq. (1) works for bivariate (i.e., dimension $n = 2$) causality analysis, which fulfills our purpose of investigating the causal interactions between SST and SHF. For multivariate ($n \geq 2$) time series causality analysis, the readers are referred to Liang (2021).

Also note that, by only knowing $T_{2\to1}$, one cannot tell how important x_2 is with respect to the entropy change of x_1 (denoted as dH_1/dt). This is because the magnitudes of $T_{2\to1}$ and dH_1/dt may both differ from case to case. Large magnitude of $T_{2\to1}$ does not necessarily imply large contribution from x_2, and vice versa. This indicates the necessity of the normalization of IF (just as the covariance does in correlation analysis). Liang (2015) proposed a normalization procedure. For instance, dH_1/dt consists of three components:

$$\frac{dH_1}{dt} = \frac{dH_1^*}{dt} + T_{2\to1} + \frac{dH_1^{\text{noise}}}{dt}, \tag{2}$$

where dH_1^*/dt, $T_{2\to1}$, and dH_1^{noise}/dt are the contributions from x_1 itself, x_2, and the noise, respectively. Liang (2015) used $Z_1 = |dH_1^*/dt| + |T_{2\to1}| + |dH_1^{\text{noise}}/dt|$ as the normalizer and obtained the normalized form of $T_{2\to1}$ as

$$\tau_{2\to1} = \frac{T_{2\to1}}{Z_1}. \tag{3}$$

If $\tau_{2\to1} = 0\%$, then x_2 exerts no impact on x_1; otherwise, x_2 is causal to x_1. Ideally, if $|\tau_{2\to1}| = 100\%$, then the entropy evolution of x_1 is totally due to the influence from x_2. Positive or negative $\tau_{2\to1}$ corresponds to either x_2 contributing to the increase or decrease of the entropy of x_1. In this study, since we concern the causal strength between air–sea interaction variables, we only need to consider the magnitude of the normalized IF.

The statistical errors are computed as follows. For the simple climate model analyzed in section 3, the error of a correlation/causality is shown in one standard deviation from the ensemble mean of 1000 simulations (realizations). For the real-world application in section 4, since only one realization is available, the significance of $T_{2\to1}$ is tested by computing the Fisher information matrix $\mathbf{I} = (I_{ij})$:

$$I_{ij} = -\frac{1}{N}\sum_{n=1}^{N}\frac{\partial^2 \log \rho(\mathbf{x}_{n+1}|\mathbf{x}_n;\,\boldsymbol{\theta})}{\partial\theta_i\partial\theta_j}, \tag{4}$$

where N is the sample size of the time series and n is the time step, $\mathbf{x} = (x_1, x_2)$, $\boldsymbol{\theta}$ is the vector of IF-related parameters to be estimated, and $\rho(\mathbf{x}_{n+1}|\mathbf{x}_n)$ is a Gaussian for a linear model. It has been established in Liang (2014) that $\mathbf{I}^{-1}/N$ is the covariance matrix of $\boldsymbol{\theta}$. Given a level, the significance of an estimated IF can be tested. More details can be found in Liang (2014).

b. Observational data

In this study, the National Oceanic and Atmospheric Administration (NOAA) optimum interpolation (OI) SST, version 2 (Reynolds et al. 2007), and the Institut Francais pour la Recherche et l'Exploitation del la Mer (IFREMER) turbulent flux estimates, version 4.1 (Bentamy 2019), are used. Both datasets have a horizontal resolution of 0.25° in longitude and latitude and a daily temporal resolution extending from 1992 to 2018.

The IFREMER sensible and latent heat fluxes are derived using the COARE 3.0 bulk algorithm (Fairall et al. 2003). The bulk variables are estimated from an improved specific air humidity retrieval scheme (Bentamy 2019), wind retrievals from all available scatterometers during 1992–2018 (Bentamy et al. 2017b), and the NOAA OI SST and the ERA-Interim air temperature (Simmons et al. 2006). Comprehensive comparison with independent mooring observations indicates that the IFREMER product has a good performance in reproducing the observed spatiotemporal characteristics of turbulent heat fluxes in the global ocean (Bentamy et al. 2017a; Bentamy 2019).

Following previous studies (e.g., Bishop et al. 2017), SHF is defined as the sum of turbulent sensible and latent heat fluxes, with positive value associated with heat release from the ocean to the atmosphere, and vice versa. The climatological annual cycles of SST and SHF are removed prior to the causality analysis, because otherwise a trivial component of IF associated with the annual cycle would merge into the result. The input time series are also linearly detrended before the analysis, although the results are almost unaltered whether or not the linear trends are removed.

3. A stochastic coupled model

a. Model description

In this section, we use a stochastic climate model to demonstrate that the IF-based causality formalism can robustly reveal the causal relationships between the ocean and atmosphere. The model was first introduced by Barsugli and Battisti (1998) with atmospheric white noise forcing. Later, Bishop et al. (2017) added oceanic noise to the model. The equations are as follows:

$$\frac{dT_a}{dt} = \alpha(T_o - T_a) - \gamma_a T_a + N_a \quad \text{and} \tag{5}$$

$$\frac{dT_o}{dt} = \beta(T_a - T_o) - \gamma_o T_o + N_o, \tag{6}$$

where T_a and T_o are, respectively, the near-surface air temperature and the SST, and N_a and N_o are, respectively, the white noise forcings of the atmosphere and ocean, which are given by a Gaussian random temperature anomaly between ±1°C multiplied by a forcing frequency of the atmosphere and ocean, i.e., ω_a and ω_o, respectively. The parameter values in the above equations are listed in Table 1. By convention (e.g., Barsugli and Battisti 1998; Wu et al. 2006; Bishop et al. 2017), SHF (q) is represented as the air–sea temperature difference in the model, i.e., $q = \alpha(T_o - T_a)$. After some simple algebraic operations, we can obtain the coupled equations for q and T_o:

$$\frac{dq}{dt} = -(\alpha + \beta + \gamma_a)q - \alpha(\gamma_o - \gamma_a)T_o + \alpha(N_o - N_a) \quad \text{and} \tag{7}$$

$$\frac{dT_o}{dt} = -\frac{\beta}{\alpha}q - \gamma_o T_o + N_o. \tag{8}$$

As in Bishop et al. (2017), the above equations are solved numerically using a forward difference scheme with a time

TABLE 1. Standard parameters (s^{-1}) in the stochastic model. The parameter values were used to describe the midlatitude air–sea interactions in previous studies (e.g., Barsugli and Battisti 1998; Bishop et al. 2017).

Parameter	Meaning	Value
α	Exchange coefficient divided by the heat capacity of the atmosphere	2.39×10^{-6}
β	Exchange coefficients divided by the heat capacity of the ocean	1.195×10^{-7}
γ_a	Radiative damping coefficient for the atmosphere	2.8×10^{-7}
γ_o	Radiative damping coefficient for the ocean	9.5×10^{-9}
ω_a	Forcing frequency of the atmosphere	1×10^{-5}
ω_o	Forcing frequency of the ocean	2×10^{-6}

step size of 1 day and initialized with zero amplitudes of q and T_o. For each case shown below, we run 1000 simulations, each having a length of 60 000 days. The error of a correlation/causality is shown in one standard deviation.

b. Lagged correlation analysis

Figure 1 shows the lagged correlations between time series of SST and SHF generated by the model. For comparison, we show the results calculated from both the monthly averaged data and the original daily sampled data, the former of which is commonly used to estimate the SST–SHF lead–lag relationships. In agreement with previous studies (e.g., Wu et al. 2006; Bishop et al. 2017), the two prevailing regimes of atmosphere forcing ocean and ocean forcing atmosphere are well captured by using monthly averaged times series of SST and SHF. When only atmospheric noise is presented (i.e., $\omega_o = 0$), the correlation between SST tendency and SHF is large and negative at zero lag (correlation coefficient $r = -0.81$; red line in Fig. 1a), whereas that between SST and SHF is very weak at zero lag ($r = -0.07$; blue line in Fig. 1a). The maximum negative correlation between SHF and SST occurs when SHF leads SST by 1 month, indicating that SHF tends to drive heat loss from the ocean. In contrast, when only oceanic noise is presented (i.e., $\omega_a = 0$), there is a large positive correlation between SST and SHF at near-zero lag (Fig. 1b). The maximum positive correlation between SHF and SST tendency occurs when the SST tendency leads the SHF by 1 month,

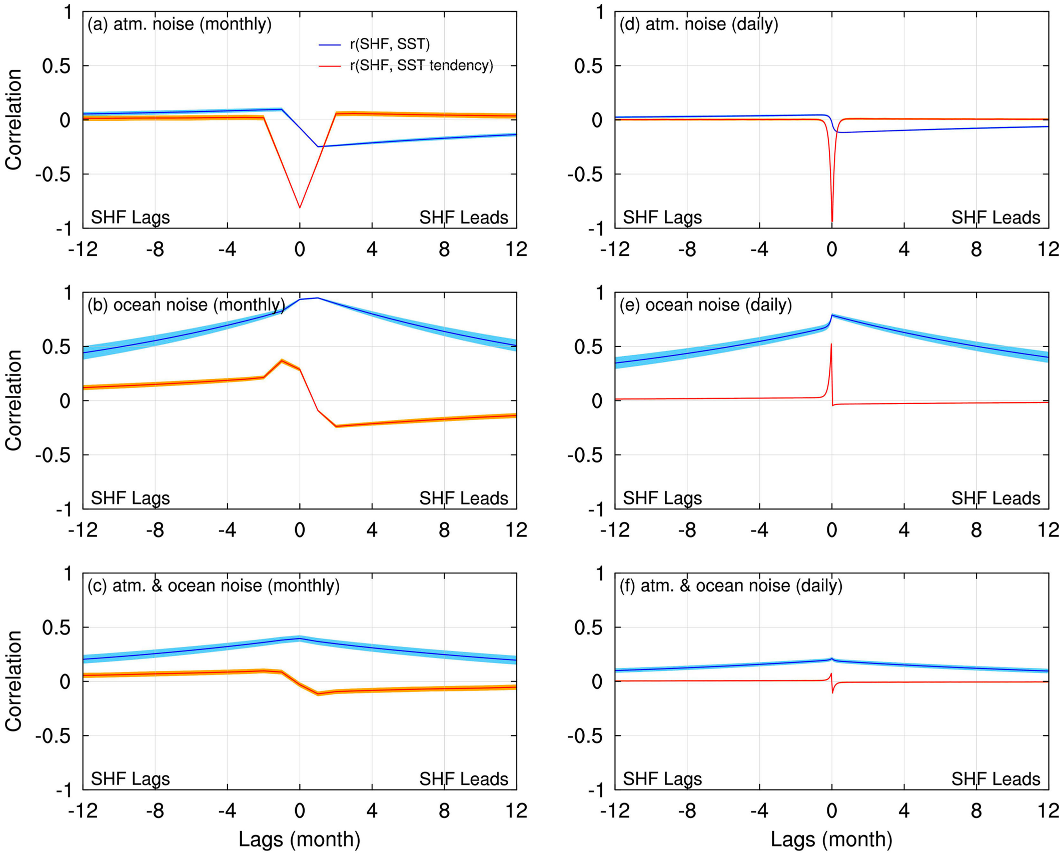

FIG. 1. Lagged correlations between SST and SHF (blue) and between SST tendency and SHF (red) from the stochastic coupled model. A positive lag means that the SHF time series takes the lead. The solid line stands for the ensemble mean, and the error envelope represents the standard deviation from the mean. (a)–(c) Results calculated from monthly data for the atmospheric noise-only case, the oceanic noise-only case, and the atmospheric and oceanic noises case, respectively. (d)–(f) As in (a)–(c), but for results calculated from daily data.

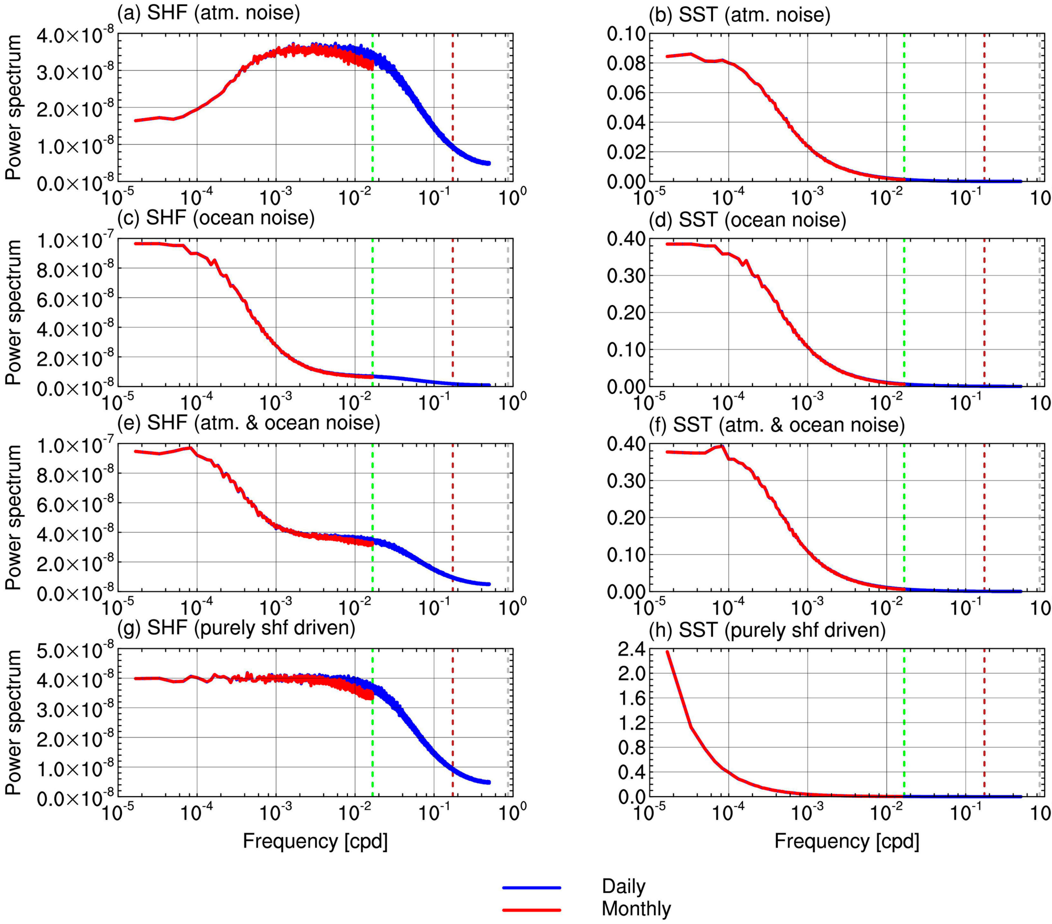

FIG. 2. Frequency spectra of (left) SHF and (right) SST. Blue line and red line represent spectrum calculated from the daily and monthly data, respectively. Green, brown, and gray vertical lines denote 1/2 month^{-1} (Nyquist frequency of the monthly averaged data), 2×10^{-6} s^{-1} (forcing frequency of the oceanic noise), and 1×10^{-5} s^{-1} (forcing frequency of the oceanic noise), respectively. (a),(b) The atmospheric noise-only case; (c),(d) the oceanic noise-only case; (e),(f) the atmospheric and oceanic noises case; (g),(h) the purely SHF-driven case.

implying that the ocean functions to warm the atmosphere. When both the atmospheric and oceanic noises are included in the model, the positive simultaneous SST–SHF correlation becomes much smaller than that with pure oceanic noise (Fig. 1c).

The above results based on monthly mean data only provide characteristics of air–sea interaction on time scales longer than 2 months (the Nyquist frequency of the monthly averaged data is 1/2 month^{-1}). To see the coupling on the submonthly time scale, we show in Figs. 1d–f the lagged correction using daily time series. For the atmospheric noise-only case, the negative correlation between SST tendency and SHF decays drastically in a few lag days (Fig. 1d). This means

TABLE 2. Normalized IFs (in absolute value and written as a percentage) between SHF and SST using daily and monthly data and 30-day low-pass and 60-day low-pass filtered data for various cases. A zero-phase Butterworth filter is applied to the daily data to obtain the low-pass filtered data. The errors shown are one standard deviation.

	Daily data		Monthly data		30-day low-pass filtered data		60-day low-pass filtered data	
	$\lvert\tau_{\mathrm{SHF}\rightarrow\mathrm{SST}}\rvert$	$\lvert\tau_{\mathrm{SST}\rightarrow\mathrm{SHF}}\rvert$	$\lvert\tau_{\mathrm{SHF}\rightarrow\mathrm{SST}}\rvert$	$\lvert\tau_{\mathrm{SST}\rightarrow\mathrm{SHF}}\rvert$	$\lvert\tau_{\mathrm{SHF}\rightarrow\mathrm{SST}}\rvert$	$\lvert\tau_{\mathrm{SST}\rightarrow\mathrm{SHF}}\rvert$	$\lvert\tau_{\mathrm{SHF}\rightarrow\mathrm{SST}}\rvert$	$\lvert\tau_{\mathrm{SST}\rightarrow\mathrm{SHF}}\rvert$
Atmospheric noise only	40.8 ± 1.6	0.1 ± 0.0	16.1 ± 1.6	0.5 ± 0.1	47.7 ± 0.5	4.2 ± 0.1	48.8 ± 0.4	12.2 ± 0.4
Purely SHF driven	100.0 ± 0.	0.0 ± 0.0	17.1 ± 16.1	0.0 ± 0.0	96.9 ± 7.6	0.1 ± 0.1	94.8 ± 9.8	0.4 ± 0.3
Oceanic noise only	29.2 ± 9.0	27.5 ± 1.7	45.8 ± 0.5	36.1 ± 1.7	49.9 ± 0.0	50.0 ± 0.0	50.0 ± 0.0	50.0 ± 0.0
Atmospheric and oceanic noises	28.2 ± 4.0	2.2 ± 0.3	8.8 ± 3.9	9.5 ± 1.4	48.4 ± 4.5	6.6 ± 0.9	47.4 ± 7.3	11.2 ± 1.7

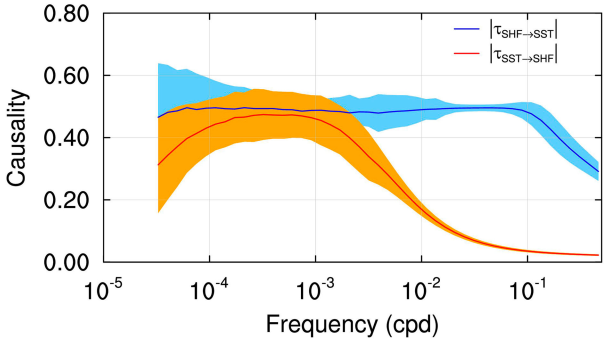

FIG. 3. Temporal-scale-dependent characteristics of $|\tau_{SHF\to SST}|$ (blue line) and $|\tau_{SST\to SHF}|$ (red line) estimated from the stochastic model with both atmospheric and oceanic noises. The solid line stands for the ensemble mean of 1000 simulations, and the error envelope represents the standard deviation from the ensemble mean.

that the influence of atmospheric noise (i.e., synoptic transients) on the SST only lasts for a couple of days. Similarly, the atmosphere's response to abnormal SST signals is also very quick (see the large positive SST tendency–SHF correlation at lag −1 day in Fig. 1e), much shorter than 1 month as suggested by the monthly mean result. Also, the simultaneous correlations between SST and SHF for oceanic noise-only case and the atmospheric and oceanic noises case are reduced using daily data (Figs. 1c,f) as compared to the monthly one (Figs. 1b,e). This is because the simultaneous correlation is mostly determined by the low-frequency part of spectrum (Fig. 2). Removing the synoptic noise will therefore lead to a higher correlation with monthly smoothed data than the daily data. These results are consistent with previous discussions on the effects of data smoothing on the cross correlations between SST and atmospheric variables (e.g., Frankignoul and Hasselmann 1977; Deser and Timlin 1997; Frankignoul et al. 1998).

c. *Causality analysis*

From the previous subsection, we have seen that under circumstances where both SHF–SST and SHF–SST tendency correlations are weak, one cannot determine which air–sea coupling regime is more dominant. In the following, we employ the IF-based causality analysis to quantify the causal linkage between SST and SHF in the stochastic coupled model.

Table 2 summarizes the rates of normalized IFs between the two variables for different cases. We first present the results using daily time series. In the case of atmospheric noise forcing only (i.e., $N_o = 0$), the causality is almost one way from SHF to SST. The influence from SHF accounts for about 40.8% of the SST entropy change, whereas SST's impact on SHF is negligible ($|\tau_{SST\to SHF}| = 0.1\%$). Note that although in this case the model is only driven by atmospheric noises, the IF from SHF to SST does not equal to 100% since SST is not only dependent on SHF but also dependent on the damping process $-\gamma_o T_o$ [see Eq. (8)]. Now, if we let $\gamma_a = \gamma_o = 0$ and $\omega_o = 0$, Eqs. (7) and (8) are reduced to

(a) $|\tau_{SHF\to SST}|$

(b) $|\tau_{SST\to SHF}|$

(c) $\log(|\tau_{SHF\to SST}|/|\tau_{SST\to SHF}|)$

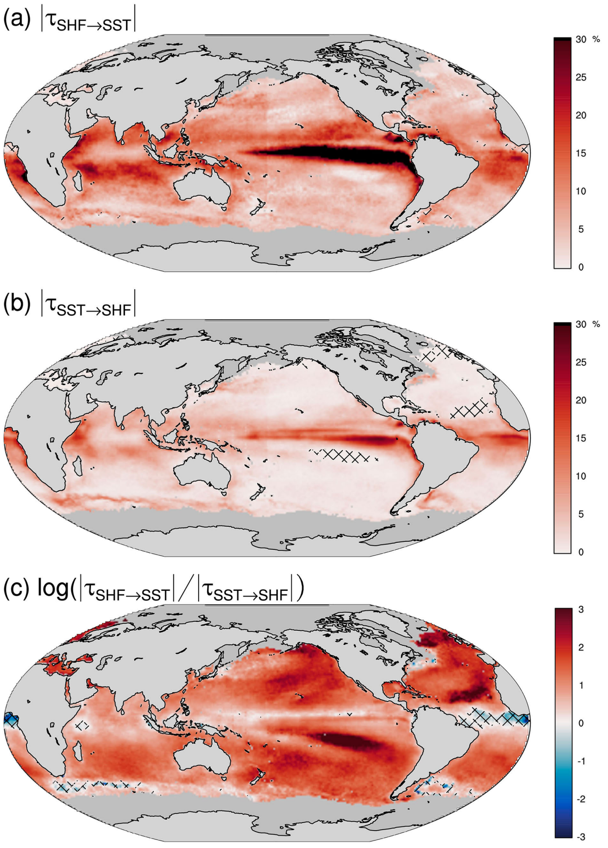

FIG. 4. Global patterns of normalized IF (in absolute value and written as a percentage) (a) from SHF to SST ($|\tau_{SHF\to SST}|$) and (b) from SST to SHF ($|\tau_{SST\to SHF}|$). Gray grid cells indicate missing values of the observational data. Hatched regions in (a) and (b) denote regions where the estimated IF is not significant at the 99% confidence level. (c) Natural logarithm of the ratio of $|\tau_{SHF\to SST}|$ to $|\tau_{SST\to SHF}|$. Hatched regions in (c) are regions where $|\tau_{SST\to SHF}|$ is greater than $|\tau_{SHF\to SST}|$. The minor discontinuity at the date line in (a) and (b) is caused by the discontinuity in the OI SST fields.

$$\frac{dq}{dt} = -(\alpha + \beta + \gamma_a)q - \alpha N_a \quad \text{and} \tag{9}$$

$$\frac{dT_o}{dt} = -\frac{\beta}{\alpha}q. \tag{10}$$

Clearly, in this case, only q drives T_o [see Eq. (10)], but not vice versa. By the IF-based formula, $|\tau_{SHF\to SST}| = 100\%$ and $|\tau_{SST\to SHF}| = 0\%$, which give the result just as one would expect. Note that the SST time series in this case exhibits very low-frequency trend (see the spectrum of SST in Fig. 2h). To see whether the IF can be faithfully estimated for time series with trends, we also calculate the running IFs using a 10 000-day window and find that the one-way causality holds perfectly well throughout the entire simulation period (not shown). This indicates that the IF estimation is fairly accurate.

Different from the scenario in the atmospheric noise-only case, when the model only contains stochastic forcing from the ocean, the IF from SHF to SST becomes comparable to

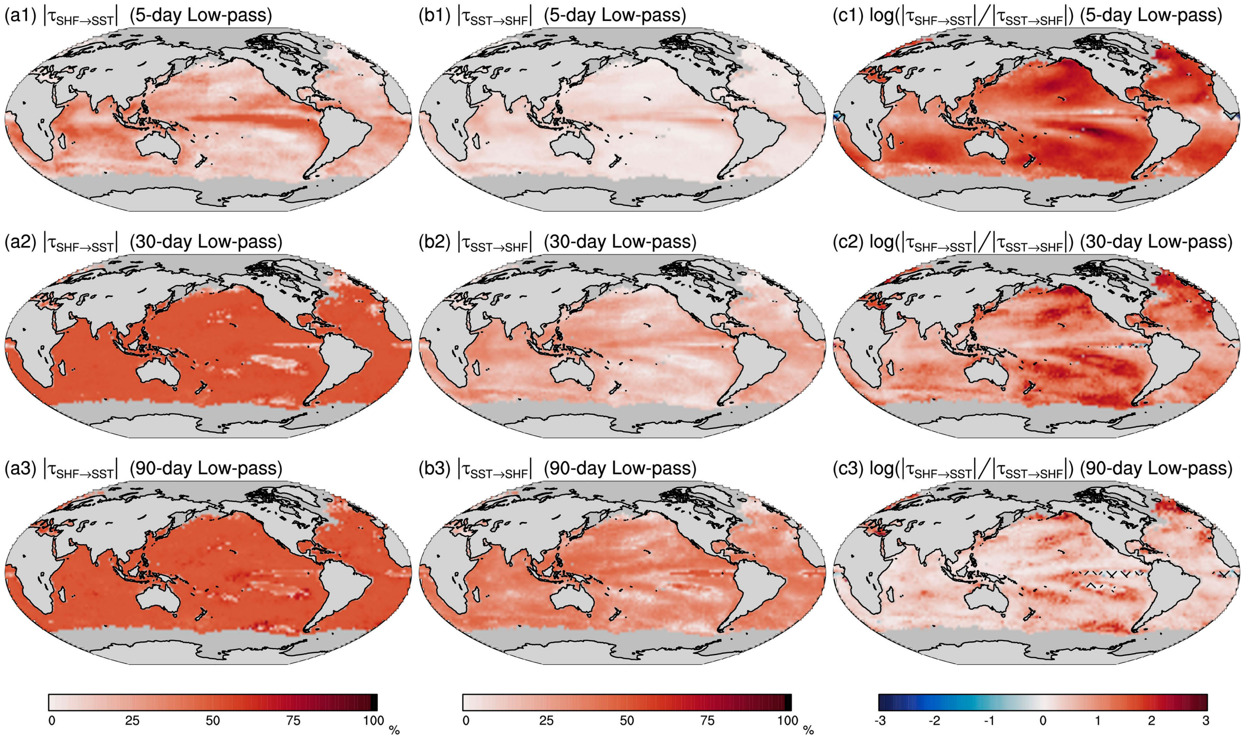

FIG. 5. As in Fig. 4, but for the temporally low-pass fields of SST and SHF. The cutoff periods are chosen as 5, 30, and 90 days, labeled as 1–3 in each subfigure. Hatched regions in (c) are regions where $|\tau_{SST\to SHF}|$ is greater than $|\tau_{SHF\to SST}|$.

the reverse flow from SST to SHF (Table 2). Even though the coupled model is purely forced by oceanic noise (e.g., mesoscale eddies and fronts), the information transferring from SHF can still account for about one-third of the SST entropy changes. The remaining processes contributing to the SST entropy changes include the damping process and the oceanic stochastic forcing [see Eq. (8)]. Note that the exclusion of atmospheric noise forcing does not necessarily imply that the magnitude of $|\tau_{SHF\to SST}|$ must be lower than that of $|\tau_{SST\to SHF}|$. The above result indicates that the SHF and SST are mutually causal when the model only contains stochastic forcing from the ocean. This is consistent with previous findings that when the oceanic noise is strong, the SHF variability is mainly driven by SST, and in turn, SHF acts to damp the SST anomaly (e.g., Bishop et al. 2017; Small et al. 2019).

Interestingly, when both noises from the atmosphere and ocean are included in the model, a significant asymmetry of causality is observed, i.e., the IF from SHF to SST is much larger than the reverse flow from SST to SHF ($|\tau_{SHF\to SST}| = 28.2\% \pm 4.0\%$ vs $|\tau_{SST\to SHF}| = 2.2\% \pm 0.3\%$). The drop of the magnitude of $|\tau_{SST\to SHF}|$ is caused by the fact that the atmospheric noise forcing makes a larger contribution to the SHF variability when the model includes atmospheric noise (i.e., the weather system). This is consistent with previous results that SHF is dominantly driven by atmospheric variability in the extratropical ocean at regions away from strong current systems (e.g., Small et al. 2019).

When the monthly averaged data are used, the causality estimations are quite different from those using daily data. For the cases where atmospheric noises are included, the IF from monthly mean SHF to monthly mean SST reduces significantly as compared to the daily scenario (Table 2). To see whether such a reduction of $|\tau_{SHF\to SST}|$ in the monthly mean case reflects the time-scale dependence of the causality, we use low-pass filters to remove the synoptic variability from the original daily time series of SHF and SST. We find that the IF from low-pass daily SHF to low-pass daily SST increases rather than decreases as compared to those estimated from the original daily time series (Table 2). To further understand this discrepancy, we interpolate the monthly mean data back to the daily resolution and find that the result is comparable with the low-pass data (not shown). This indicates that the different result using monthly mean and daily mean data is actually caused by the sampling time step size. To further test whether the causality estimation is influenced by a more frequent sampling, we generate the model using hourly time step and find that the IFs estimated in this way are very similar to the daily scenario (not shown). The above results indicate the necessity to use daily or more frequent sampling data to estimate the causality between SHF and SST in the stochastic model.

To further investigate the time-scale dependence of causality, we employed low-pass filters with various cutoff frequencies to the daily sampled data and then calculate $|\tau_{SHF\to SST}|$ and $|\tau_{SST\to SHF}|$ at each cutoff frequency. Figure 3 shows the

IFs as a function of low-pass filter cutoff frequency, estimated from the model with both atmospheric and oceanic noises. It can be seen that $|\tau_{\mathrm{SHF}\rightarrow\mathrm{SST}}|$ increases significantly with the increasing period in the range of short time-scales (2–10 days) and remains almost unchanged with longer time scales (>10 days). In contrast, $|\tau_{\mathrm{SST}\rightarrow\mathrm{SHF}}|$ increases significantly with the increasing period over the time scales of 1 month–3 years. For time scales longer than 10 years, $|\tau_{\mathrm{SST}\rightarrow\mathrm{SHF}}|$ decreases with the increasing period. In the appendix, we further show the sensitivity of causality estimations to the six parameters (i.e., ω_a, ω_o, γ_a, γ_o, α, and β) in the stochastic model.

(a) $|\tau_{\mathrm{SHF}\rightarrow\mathrm{SST}}|$ (90-day High-pass)

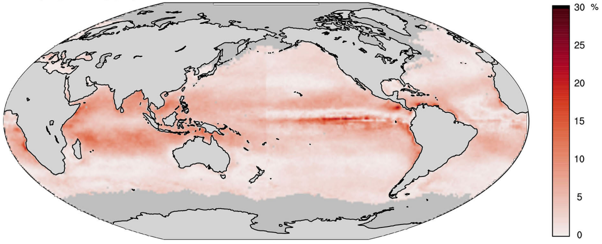

(b) $|\tau_{\mathrm{SST}\rightarrow\mathrm{SHF}}|$ (90-day High-pass)

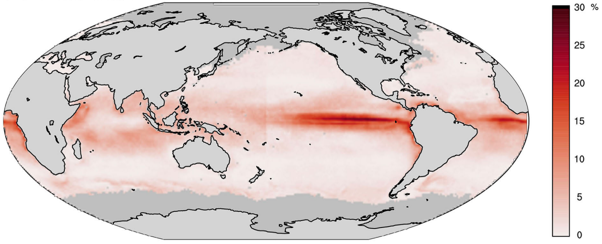

(c) $\log(|\tau_{\mathrm{SHF}\rightarrow\mathrm{SST}}|/|\tau_{\mathrm{SST}\rightarrow\mathrm{SHF}}|)$ (90-day High-pass)

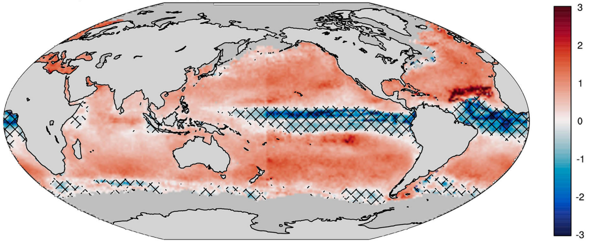

FIG. 6. As in Fig. 4, but for the temporally high-pass (cutoff period: 90 days) fields of SST and SHF. Hatched regions in (c) are regions where $|\tau_{\mathrm{SST}\rightarrow\mathrm{SHF}}|$ is greater than $|\tau_{\mathrm{SHF}\rightarrow\mathrm{SST}}|$.

4. Causality from satellite observations

The above analysis demonstrates the usefulness of the IF-based causality formalism for identifying the causal direction and causal strength between SHF and SST in a highly idealized stochastic model. In this section, we use eddy-permitting global daily observational records of SHF and SST to analyze the causality between the two variables in the real world, with emphasis on its global distribution, spatial- and temporal-scale dependences, and seasonal variations.

a. Global pattern

Figures 4a and 4b show the global patterns of $|\tau_{\mathrm{SHF}\rightarrow\mathrm{SST}}|$ and $|\tau_{\mathrm{SST}\rightarrow\mathrm{SHF}}|$ estimated from the observational daily records of SHF and SST over the period of 1992–2018, respectively. As expected, both metrics reach maxima in the tropics, indicating that the ocean and atmosphere are strongly coupled there. In the eastern equatorial Pacific, the maximum contribution of SHF to the SST entropy variation is over 50%, whereas the maximum contribution of SST to the SHF entropy variation is over 30%. In the tropical Indian Ocean, enhanced causalities from both directions are located at the northern and southern flanks of the equator. These results are generally in line with Docquier et al. (2023) using monthly data.

Away from the tropics, the magnitudes of both metrics drop significantly, with contributions typically less than 10%. As will be seen in section 4b, the inclusion of synoptic variability in the daily data leads to small values of IF in the extratropics. There is notable amount of information flowing from SST to SHF in frontal regions such as the WBCs and the ACC. These are regions of sharp SST gradients, where the atmosphere is strongly affected by the ocean (e.g., Small et al. 2008; Seo et al. 2023). This point will be further discussed in section 4c.

The relative importance of causalities between SHF and SST is provided by calculating the ratio of $|\tau_{\mathrm{SHF}\rightarrow\mathrm{SST}}|$ to $|\tau_{\mathrm{SST}\rightarrow\mathrm{SHF}}|$ (Fig. 4c). The result is shown in logarithm such that negative values imply that SST drives SHF more strongly than SHF drives SST, and vice versa. The $|\tau_{\mathrm{SHF}\rightarrow\mathrm{SST}}|$ is considerably larger than $|\tau_{\mathrm{SST}\rightarrow\mathrm{SHF}}|$ throughout most of the extratropical oceans, especially in the central and eastern parts of the subtropical–midlatitude North Pacific, South Pacific, and North Atlantic, indicating that SHF drives the SST variability more than vice versa. This asymmetric causal relation (i.e., $|\tau_{\mathrm{SHF}\rightarrow\mathrm{SST}}| > |\tau_{\mathrm{SST}\rightarrow\mathrm{SHF}}|$) estimated from observations seems to be consistent with the stochastic model described above with both atmospheric and oceanic noises presented.

A lower ratio is found in the tropics and extratropical frontal zones due to the enhanced impact of SST variability to the overlying atmosphere in these regions. It is worth noting that even in most area of these regions, $|\tau_{\mathrm{SHF}\rightarrow\mathrm{SST}}|$ is still larger than $|\tau_{\mathrm{SST}\rightarrow\mathrm{SHF}}|$, except for a few areas in the tropical Atlantic, the Southern Ocean Agulhas current region, etc. (Fig. 4c). We will show in section 4c that the dominance of $|\tau_{\mathrm{SHF}\rightarrow\mathrm{SST}}|$ over $|\tau_{\mathrm{SST}\rightarrow\mathrm{SHF}}|$ is due to the dominance of $|\tau_{\mathrm{SHF}\rightarrow\mathrm{SST}}|$ on very large scales (>20°). Regarding spatial scales < 10°, on the contrary, there is a dominance of $|\tau_{\mathrm{SST}\rightarrow\mathrm{SHF}}|$ over $|\tau_{\mathrm{SHF}\rightarrow\mathrm{SST}}|$.

b. Dependence of causality on temporal scales

Results shown in section 4a are based on daily time series, which reveal the characteristics of couple variability with periods longer than 2 days (the Nyquist frequency of the daily data is 1/2 day^{-1}). In this subsection, we further investigate the temporal-scale-dependent characteristics of the causality. As in section 3c, we employ a zero-phase Butterworth filter with various cutoff frequencies to the daily time series at each grid. For each cutoff frequency, we obtain the smoothed

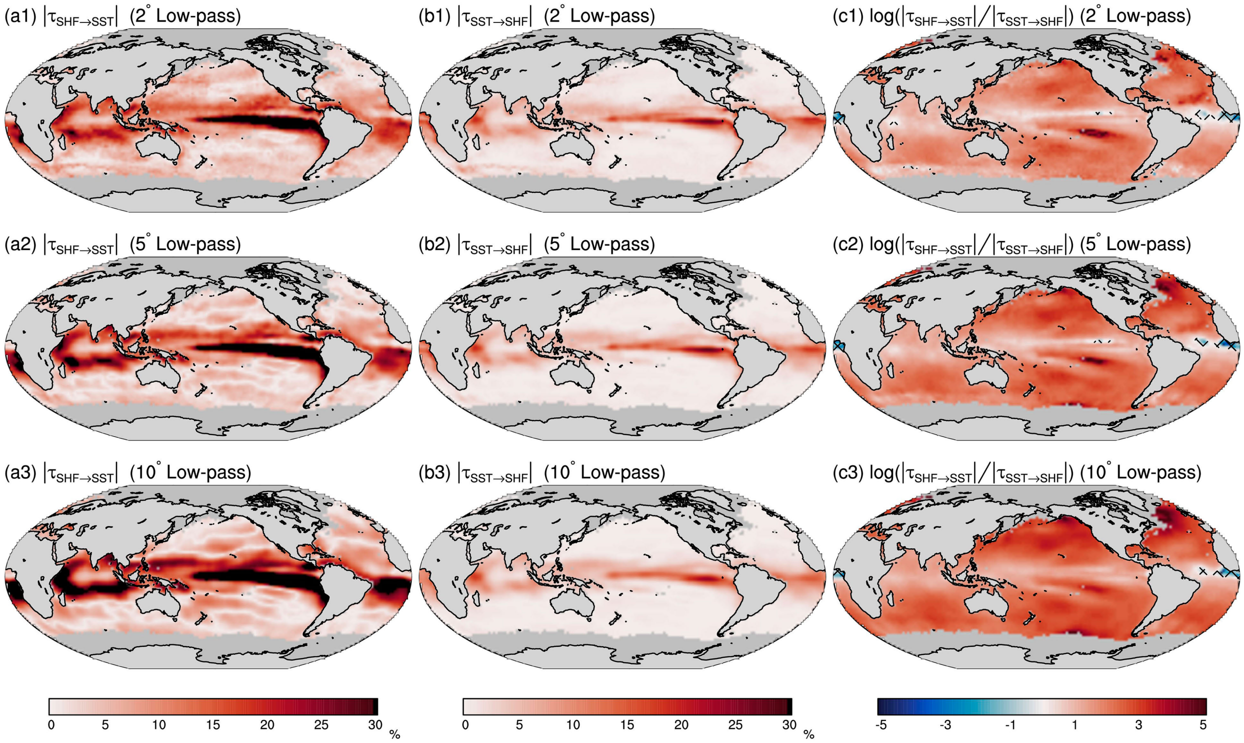

FIG. 7. As in Fig. 4, but for the spatially low-pass fields of SST and SHF. The cutoff lengths of the low-pass boxcar filter are chosen as 1°, 5°, and 10°, labeled as 1–3 in each subfigure. Hatched regions in (c) are regions where $|\tau_{SST\to SHF}|$ is greater than $|\tau_{SHF\to SST}|$.

(low-pass) fields of SST and SHF and then calculate the IFs using Eq. (1).

Figure 5 shows the causality between SHF and SST as a function of time scales. A general observation is that both $|\tau_{SHF\to SST}|$ and $|\tau_{SST\to SHF}|$ get larger with increasing time scale. The most drastic increase of $|\tau_{SHF\to SST}|$ occurs on time scales shorter than 1 month (Fig. 5a). For the time scale longer than 1 month, the magnitude of $|\tau_{SHF\to SST}|$ does not change much, with contribution greater than 50% over most of the global ocean. In contrast, the magnitude of $|\tau_{SST\to SHF}|$ is quite low on synoptic time scales compared to $|\tau_{SHF\to SST}|$, indicative of an atmosphere-driven regime at these high-frequency time scales. A rapid increase is seen between time scale of 1 and 3 months (Fig. 5b). For time scales longer than 90 days, $|\tau_{SHF\to SST}|$ does not increase further (not shown), with contribution greater than 40% over much of the global ocean. From the ratio maps (Fig. 5c), one can see that the influence of SST on the atmosphere increases with time scales, indicating that the ocean plays a more important role in air–sea interactions at longer time scales.

Regarding the SST–SHF causality at short time scales (Fig. 6), the IF from SHF to SST is larger than the reverse flow over most of the global ocean except in the eastern-to-central equatorial Pacific, the equatorial Atlantic, and the ACC (Fig. 6c). Note that we have tested the high-pass cutoff periods varying from 10 to 180 days and find that the results are similar. In particular, the large and dominant causality from SST to SHF in the equatorial Pacific reveals the strong influence of SST variability on the surface heat fluxes modulated by the tropical instability waves (TIWs) at intraseasonal time scales (e.g., Menkes et al. 2006). In the extratropics, the ratio of $|\tau_{SHF\to SST}|$ to $|\tau_{SST\to SHF}|$ is quite large, particularly the storm-track regions (i.e., the central and eastern parts of the midlatitude ocean basins), indicative of a regime that synoptic storms drive the SST variability rather than the other way around.

c. *Dependence of causality on spatial scales*

In this subsection, we further investigate the spatial-scale-dependent characteristics of the causality. As in several previous studies (e.g., Bishop et al. 2017; Small et al. 2019; Sun and Wu 2022), we employ a simple boxcar filter, with a cutoff side length increasing from 1° to 20°, to fulfill the scale separation. For each cutoff length, we obtain smoothed (low-pass) fields of SST and SHF and then calculate the IFs using Eq. (1).

Global causal structures with various smoothing lengths are shown in Fig. 7. In the tropics, the causal strength from SHF to SST generally increases with increasing spatial scales (Fig. 7a). A recent study by Sun and Wu (2022) addressed the spatial dependence of SHF–SST and SHF–SST tendency correlations. The authors found that the negative SHF–SST tendency correlation, indicative of SHF driving SST, increases with spatial scales in the tropical regions. This is consistent with our result. It is worth mentioning that the wind forcing has been recognized as an important process in the tropical air–sea interactions (e.g., McPhaden and Hayes 1991). The

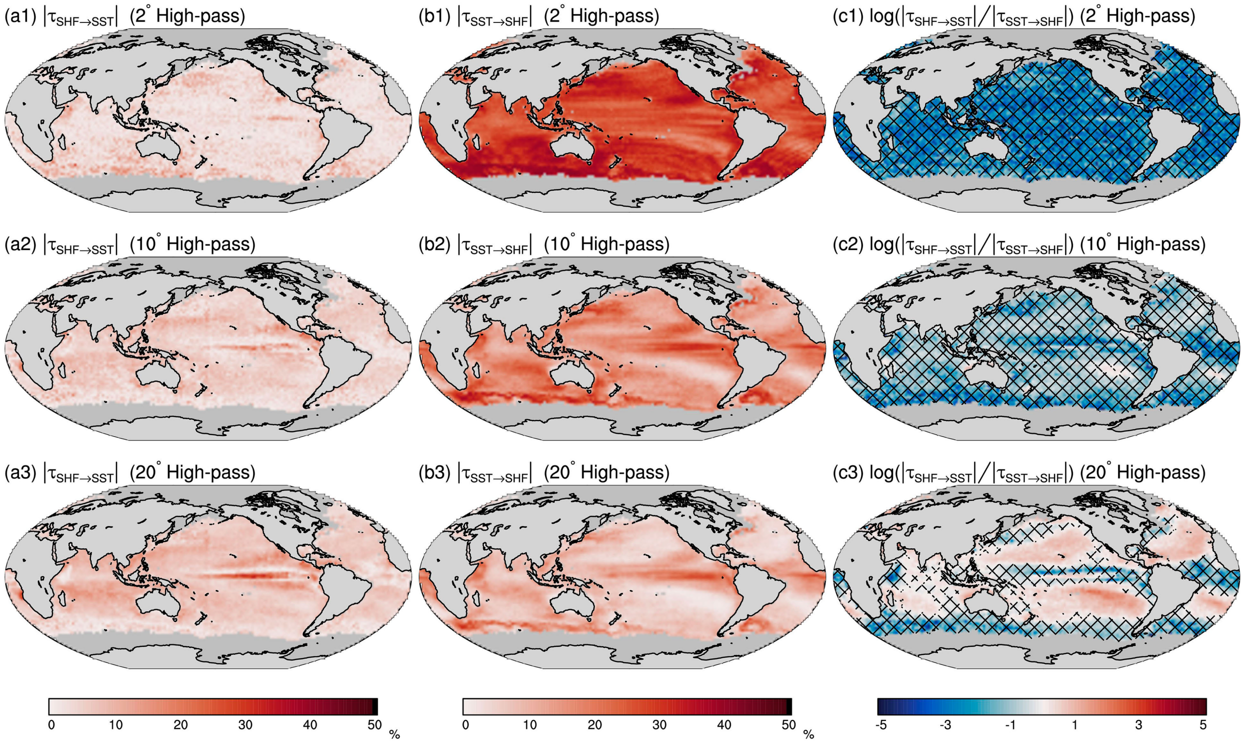

FIG. 8. As in Fig. 4, but for the spatially high-pass fields of SST and SHF. The high-pass field is obtained by subtracting the low-pass filtered field with a cutoff length from the original data. The cutoff lengths of the low-pass boxcar filter are chosen as 2°, 10°, and 20°, labeled as 1–3 in each subfigure. Hatched regions in (c) are regions where $|\tau_{SST\to SHF}|$ is greater than $|\tau_{SHF\to SST}|$.

influence of wind forcing in the SHF–SST relation is not considered in our analysis and will be the focus of a future study.

Regarding the causality from SST to SHF in the tropics, it seems not sensitive to the low-pass filter cutoff length (Fig. 7b). As a result, the ratio of $|\tau_{SHF\to SST}|$ to $|\tau_{SST\to SHF}|$ gets larger with increasing scale there (Fig. 7c). Away from the tropics, there is a reduction of $|\tau_{SST\to SHF}|$ with increasing scale in most locations, particularly in the frontal zones (Fig. 7b), leading to larger ratio of $|\tau_{SHF\to SST}|$ to $|\tau_{SST\to SHF}|$ as the spatial scale becomes larger (Fig. 7c).

In the above analysis, we have seen that smoothing the original unfiltered fields tends to reduce the ocean's impact on the overlying atmosphere in the ocean frontal zones. To further extend this point, we analyze the causality between high-pass SST and SHF, which is obtained by subtracting the low-pass filtered field with a cutoff length from the original unfiltered data. From Fig. 8, it can be seen that $|\tau_{SHF\to SST}|$ increases with larger spatial scale, whereas $|\tau_{SST\to SHF}|$ increases with smaller spatial scale. The horizontal structure of $|\tau_{SST\to SHF}|$ exhibits high values in regions of high SST gradients (Fig. 8b). For horizontal scales smaller than 10°, $|\tau_{SST\to SHF}|$ is larger than $|\tau_{SHF\to SST}|$ in most of the global ocean [see the hatched regions in Fig. 8c(2)]. For horizontal scales small than 20°, the dominance of $|\tau_{SST\to SHF}|$ over $|\tau_{SHF\to SST}|$ still exists in the equatorial regions, WBC regions, and ACC region, whereas $|\tau_{SHF\to SST}|$ becomes larger than $|\tau_{SST\to SHF}|$ in the interior basins. The above results indicate that SHF drives SST variability at very large spatial scales, whereas SST drives SHF at small scales, especially in regions with high SST gradients.

d. *Seasonality*

The causalities are also expected to change with time. In this study, we only focus on their seasonality. This is done by applying Eq. (1) to time series of SST and SHF for each season. Figure 9 displays the horizontal distributions of $|\tau_{SHF\to SST}|$ and $|\tau_{SST\to SHF}|$ in the four seasons. There is a clear spatial inhomogeneity in the causality seasonality. In the eastern equatorial Pacific, $|\tau_{SHF\to SST}|$ is large throughout the year except in boreal winter months [January–March (JFM)], whereas $|\tau_{SST\to SHF}|$ does not vary significantly by season. This contrasts with the central equatorial Pacific where the SST forcing is much higher during boreal autumn [October–December (OND)] and winter (JFM) than that during spring [April–June (AMJ)] and summer [July–September (JAS)]. In the tropical Atlantic, $|\tau_{SST\to SHF}|$ has a sharp peak during the AMJ season, whereas $|\tau_{SHF\to SST}|$ remains large throughout the year. Away from the equator, the most pronounced seasonality is found in the tropical North India and subtropical western North Pacific. Both causality metrics reach maximum during the AMJ season and minimum in the OND season in this band, suggesting that the local interaction between SST and SHF is strongest in boreal spring. Over the extratropical ocean, the seasonal modulation of causality is in general quite weak, except in the Kuroshio Extension and northeastern corner of the North Pacific.

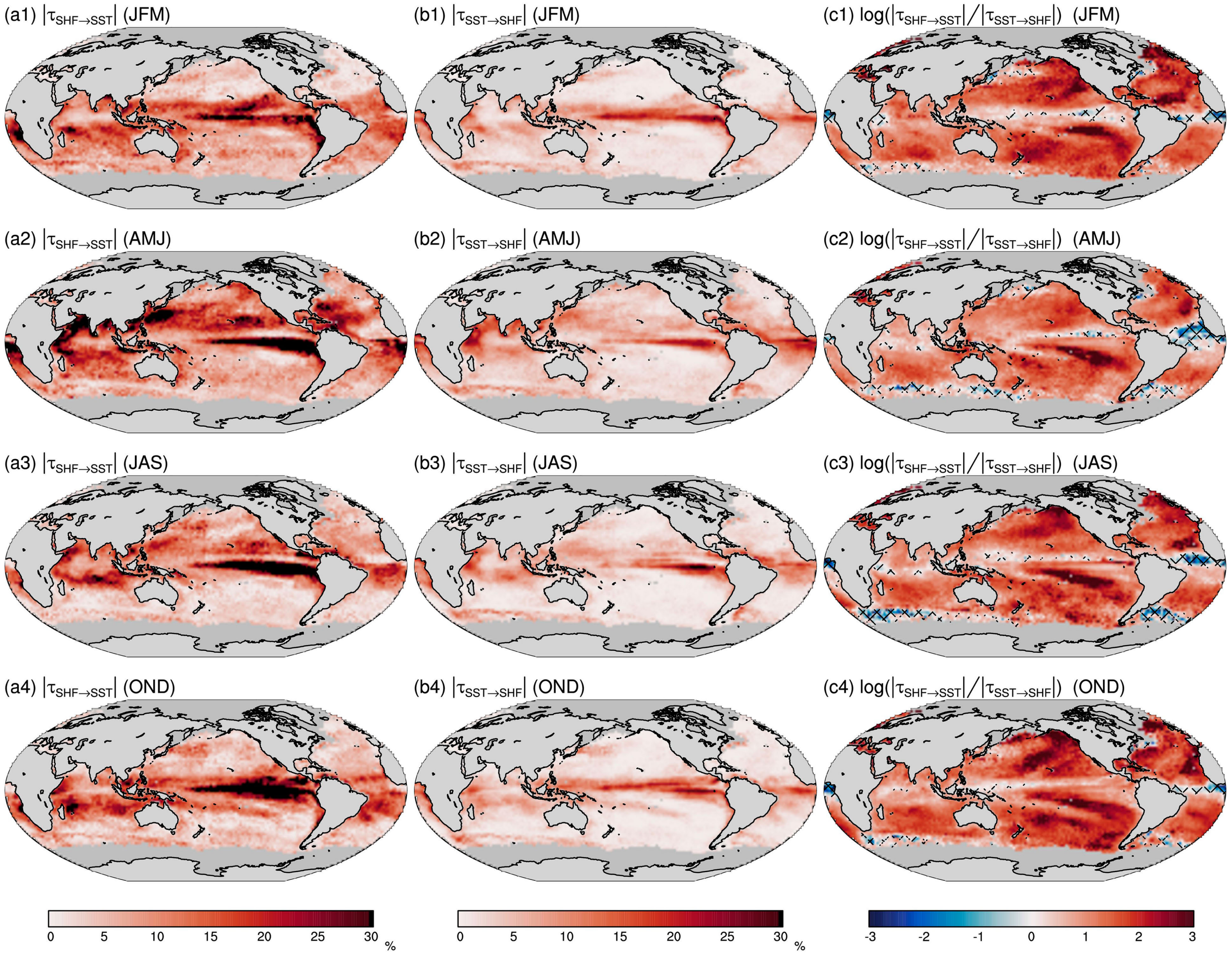

FIG. 9. As in Fig. 4, but for the boreal (a1),(b1),(c1) winter (JFM), (a2),(b2),(c2) spring (AMJ), (a3),(b3),(c3) summer (JAS), and (a4),(b4),(c4) autumn (OND). Hatched regions in (c) are regions where $|\tau_{SST\to SHF}|$ is greater than $|\tau_{SHF\to SST}|$.

The above identified seasonality of the causal relation between SST and SHF in the tropics is mainly determined by the large-scale processes. The seasonal cycles of $|\tau_{SHF\to SST}|$ and $|\tau_{SST\to SHF}|$ in the tropical ocean are almost identical to those estimated from the original unfiltered time series (not shown). The causality from SST to SHF at scales smaller than 10° dominates that from SHF to SST, and the seasonal variations in hotspots such as the WBCs and ACC are consistent with the ones estimated from the unfiltered data (not shown).

5. Summary and discussion

This study uses a novel causal inference method to understand the geographical variation, space- and time-scale dependence, and seasonality of air–sea interaction in the global oceans. The target variables are SST and SHF, which are frequently used to discriminate the dominance of atmosphere forcing or ocean forcing in idealized stochastic models as well as in the realistic coupled climate system. The causal inference method is based on the theory of IF, hence quantitative in nature (Liang 2014, 2016). An important advantage of our method, as compared to traditional approaches such as the lagged correlation analysis widely used in the field of air–sea interaction, is that it provides both the directionality and strength of causality between mutually interacting variables.

The method is first validated with a classical stochastically forced, coupled energy balance model. The cause–effect relation of the SST and SHF in the model can be faithfully revealed by the two IF metrics, i.e., $|\tau_{SHF\to SST}|$ and $|\tau_{SST\to SHF}|$, measuring the causality strength from SHF to SST and from SST to SHF, respectively. Particularly, it successfully verifies a specially designed case in which only SHF drives SST. We find that the SHF and SST are mutually causal when the model only contains stochastic forcing from the ocean. When the model includes both noise forcings from the atmosphere and ocean, a significant asymmetry of causality between SHF and SST is observed, i.e., $|\tau_{SHF\to SST}|$ is much larger than $|\tau_{SST\to SHF}|$. This because the atmospheric noise makes a larger contribution to the SHF variability when the model includes stochastic forcing from the atmosphere.

We further apply the method to the observational time series of SST and SHF at a daily temporal resolution and a

0.25° spatial resolution from 1992 to 2018. As in the stochastic model, there is an overall asymmetry of causality between the two variables in the real ocean, namely, $|\tau_{\mathrm{SHF}\rightarrow\mathrm{SST}}|$ is significantly larger than $|\tau_{\mathrm{SST}\rightarrow\mathrm{SHF}}|$ over most of the global oceans. The SST–SHF coupling is strongest in the tropics and decreases substantially in the extratropics. In ocean frontal regions near the WBCs and ACC, SST makes higher contributions to the SHF variability.

The causality is found to be scale dependent. The dominance of SHF driving SST occurs at very large scales (>20°), whereas the dominance of SST driving SHF mostly occurs at scales smaller than 10°. The causalities in both directions get larger with increasing time scale and are less asymmetric at longer time scales. The causality also exhibits strong seasonality. In the tropics, the seasonal variations of $|\tau_{\mathrm{SHF}\rightarrow\mathrm{SST}}|$ and $|\tau_{\mathrm{SST}\rightarrow\mathrm{SHF}}|$ are determined by the air–sea interaction of large-scale processes. In the extratropical frontal regions, the seasonality of the causality from SST to SHF is modulated by the seasonal changes of the mesoscale eddy variability.

One of the limitations of the present study is that we only focus on the causal relation between SST and SHF. We choose this pair of variables because it is relatively well studied in the climate community, thus allowing for a more direct comparison of our results and the known results and a demonstration of the usefulness of the IF formalism. Further studied are needed for a better understanding of the causal links between SST and the intrinsic atmospheric variability such as those presented by the air temperature, wind, and sea surface pressure.

Another noteworthy limitation is that the causality formula used in this study is based on a linear assumption. Although the formula works for the stochastic model (section 3) since the model is linear, it remains unknown to what extend the formula works for the real climate system which is nonlinear. A more general IF-based formalism is yet to be explored for nonlinear systems. Besides, the causal inference in the present study is based on the bivariate causality formalism, which is only applicable to a two-dimensional system, such as the stochastic model in section 3. In the real climate system, more air–sea variables, such as the wind, are involved. In that case, the multivariate causality formalism (Liang 2021) would be promising in disentangling the causality among multiple dimensional system. See a recent attempt by Docquier et al. (2023). This is beyond the scope of the present study and we leave it for future study.

Acknowledgments. YY thanks Dr. Yineng Rong and Dr. Huijie Xue for valuable discussions. The constructive comments by three anonymous reviewers are appreciated. YY and XSL are supported by the National Science Foundation of China (NSFC) (Grants 42276017, 42230105, and 41975064), the Southern Marine Science and Engineering Guangdong Laboratory (Zhuhai) Project (Grant SML2023SP203), and the Fundamental Research Funds for the Central Universities (Grant 20720240104). ZL's participation of this work was supported by the Natural Science Foundation of Fujian Province of China (2021J02005), the National Key R&D Program of China (2023YFE0126700 and 2022YFA1003804), and the NSFC through Grant 92258301.

Data availability statement. The OISST and the IFREMER turbulent flux estimate are available at https://data-cersat.ifremer.fr/data/heat-flux/ifremer/v4.1/daily/. The causality analysis package is available at http://www.ncoads.org/.

APPENDIX

Parameter Sensitivity of the Stochastic Model

Figure A1 presents the sensitivity of causality to the six parameters (i.e., ω_a, ω_o, γ_a, γ_o, α, and β) in the stochastic model. For each subfigure in Fig. A1, only one parameter (horizontal axis) is allowed to vary, with other five parameters fixed as the values listed in Table 1. The magnitude of IF from SST to SHF is strongly dependent on the stochastic forcing frequency. In the frequency band ranging from 10^{-6} ($\approx$11.6) to 10^{-5} s^{-1} ($\approx$1.2 day^{-1}), $|\tau_{\mathrm{SST}\rightarrow\mathrm{SHF}}|$ decreases drastically as ω_a increases (Fig. A1a) and increases drastically as ω_o increases (Fig. A1b). This means that high-frequency atmospheric stochastic forcing tends to reduce the ocean forcing in the atmosphere, and vice versa. The IF from SHF to SST is always larger than the reverse flow and does not change much in the abovementioned frequency band (Figs. A1a,b). Its magnitude drops only at very high frequencies of atmospheric forcing ($\omega_a > 10^{-5}$ s^{-1}) and very low frequencies of oceanic forcing ($\omega_o < 10^{-6}$ s^{-1}).

Regarding the damping and exchange coefficients (i.e., γ_a, γ_o, α, and β), the IF from SHF to SST seems to be more sensitive to these parameters as compared to the reverse flow. It increases with increasing γ_a or β (Figs. A1c,f) and decreases with increasing γ_o or α (Figs. A1d,e). In contrast, the IF from SST to SHF keeps a relatively low magnitude as these parameters vary, with the exception of γ_a. There is a significant increase of $|\tau_{\mathrm{SST}\rightarrow\mathrm{SHF}}|$ as γ_a increases (Fig. A1c).

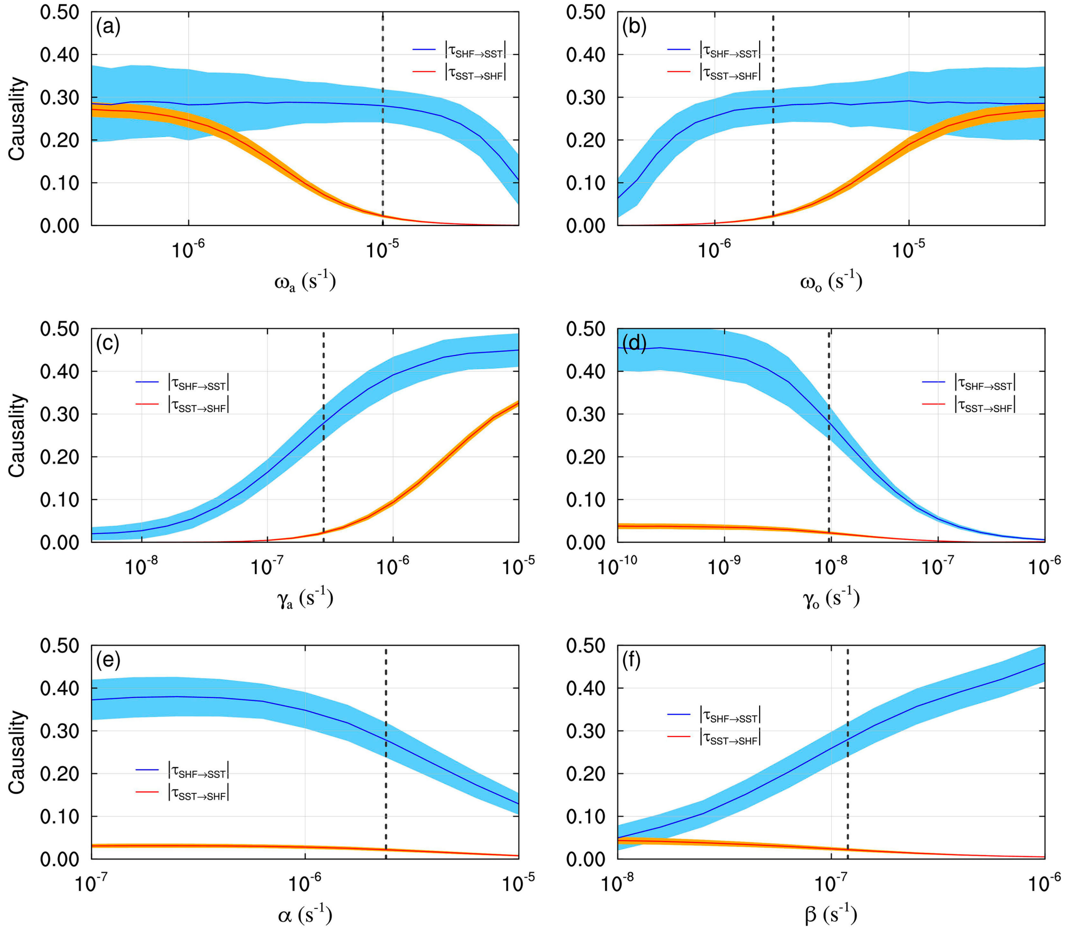

FIG. A1. (a) Normalized IFs as a function of ω_a (s^{-1}). The IF from SHF to SST $|\tau_{\mathrm{SHF}\rightarrow\mathrm{SST}}|$ is shown in blue line, and the IF from SST to SHF $|\tau_{\mathrm{SST}\rightarrow\mathrm{SHF}}|$ is shown in red line. The solid line stands for the ensemble mean, and the error envelope represents the standard deviation from the mean. (b)–(f) As in (a), but for the normalized IFs as a function of ω_o, γ_a, γ_o, α, and β, respectively. The dashed vertical line in each subfigure indicates the standard value for each parameter as listed in Table 1.

REFERENCES

Barsugli, J. J., and D. S. Battisti, 1998: The basic effects of atmosphere–ocean thermal coupling on midlatitude variability. *J. Atmos. Sci.*, **55**, 477–493, https://doi.org/10.1175/1520-0469(1998)055<0477:TBEOAO>2.0.CO;2.

Bentamy, A., 2019: Upgrading and estimation of long time series of heat fluxes from remotely sensed observations 1992–2018. IFREMER, https://data-cersat.ifremer.fr/data/heat-flux/ifremer/v4.1/.

——, and Coauthors, 2017a: Review and assessment of latent and sensible heat flux accuracy over the global oceans. *Remote Sens. Environ.*, **201**, 196–218, https://doi.org/10.1016/j.rse.2017.08.016.

——, S. A. Grodsky, A. Elyouncha, B. Chapron, and F. Desbiolles, 2017b: Homogenization of scatterometer wind retrievals. *Int. J. Climatol.*, **37**, 870–889, https://doi.org/10.1002/joc.4746.

Bishop, S. P., R. J. Small, F. O. Bryan, and R. A. Tomas, 2017: Scale dependence of midlatitude air–sea interaction. *J. Climate*, **30**, 8207–8221, https://doi.org/10.1175/JCLI-D-17-0159.1.

——, ——, and ——, 2020: The global sink of available potential energy by mesoscale air-sea interaction. *J. Adv. Model. Earth Syst.*, **12**, e2020MS002118, https://doi.org/10.1029/2020MS002118.

Bladé, I., 1997: The influence of midlatitude ocean–atmosphere coupling on the low-frequency variability of a GCM. Part I: No tropical SST forcing. *J. Climate*, **10**, 2087–2106, https://doi.org/10.1175/1520-0442(1997)010<2087:TIOMOA>2.0.CO;2.

Cayan, D. R., 1992: Latent and sensible heat flux anomalies over the northern oceans: Driving the sea surface temperature. *J. Phys. Oceanogr.*, **22**, 859–881, https://doi.org/10.1175/1520-0485(1992)022<0859:LASHFA>2.0.CO;2.

Chelton, D. B., and S.-P. Xie, 2010: Coupled ocean-atmosphere interaction at oceanic mesoscales. *Oceanography*, **23** (4), 52–69, https://doi.org/10.5670/oceanog.2010.05.

——, M. G. Schlax, M. H. Freilich, and R. F. Milliff, 2004: Satellite measurements reveal persistent small-scale features in ocean winds. *Science*, **303**, 978–983, https://doi.org/10.1126/science.1091901.

Deser, C., and M. S. Timlin, 1997: Atmosphere–ocean interaction on weekly timescales in the North Atlantic and Pacific. *J. Climate*, **10**, 393–408, https://doi.org/10.1175/1520-0442(1997)010<0393:AOIOWT>2.0.CO;2.

Docquier, D., S. Vannitsem, and A. Bellucci, 2023: The rate of information transfer as a measure of ocean–atmosphere interactions. *Earth Syst. Dyn.*, **14**, 577–591, https://doi.org/10.5194/esd-14-577-2023.

Duhaut, T. H. A., and D. N. Straub, 2006: Wind stress dependence on ocean surface velocity: Implications for mechanical energy input to ocean circulation. *J. Phys. Oceanogr.*, **36**, 202–211, https://doi.org/10.1175/JPO2842.1.

Fairall, C. W., E. F. Bradley, J. E. Hare, A. A. Grachev, and J. B. Edson, 2003: Bulk parameterization of air–sea fluxes: Updates and verification for the COARE algorithm. *J. Climate*, **16**, 571–591, https://doi.org/10.1175/1520-0442(2003)016<0571:BPOASF>2.0.CO;2.

Frankignoul, C., 1985: Sea surface temperature anomalies, planetary waves, and air-sea feedback in the middle latitudes. *Rev. Geophys.*, **23**, 357–390, https://doi.org/10.1029/RG023i004p00357.

——, and K. Hasselmann, 1977: Stochastic climate models, Part II application to sea-surface temperature anomalies and thermocline variability. *Tellus*, **29A**, 289–305, https://doi.org/10.3402/tellusa.v29i4.11362.

——, A. Czaja, and B. L'Heveder, 1998: Air–sea feedback in the North Atlantic and surface boundary conditions for ocean models. *J. Climate*, **11**, 2310–2324, https://doi.org/10.1175/1520-0442(1998)011<2310:ASFITN>2.0.CO;2.

Hasselmann, K., 1976: Stochastic climate models Part I. Theory. *Tellus*, **28**, 473–485, https://doi.org/10.1111/j.2153-3490.1976.tb00696.x.

Hristopulos, D. T., A. Babul, S. Babul, L. R. Brucar, and N. Virji-Babul, 2019: Disrupted information flow in resting-state in adolescents with sports related concussion. *Front. Hum. Neurosci.*, **13**, 419, https://doi.org/10.3389/fnhum.2019.00419.

Kalnay, E., K. C. Mo, and J. Paegle, 1986: Large-amplitude, short-scale stationary Rossby waves in the Southern Hemisphere: Observations and mechanistic experiments to determine their origin. *J. Atmos. Sci.*, **43**, 252–275, https://doi.org/10.1175/1520-0469(1986)043<0252:LASSSR>2.0.CO;2.

Kirtman, B. P., and Coauthors, 2012: Impact of ocean model resolution on CCSM climate simulations. *Climate Dyn.*, **39**, 1303–1328, https://doi.org/10.1007/s00382-012-1500-3.

Li, F., H. Sang, and Z. Jing, 2017: Quantify the continuous dependence of SST-turbulent heat flux relationship on spatial scales. *Geophys. Res. Lett.*, **44**, 6326–6333, https://doi.org/10.1002/2017GL073695.

Liang, X. S., 2008: Information flow within stochastic dynamical systems. *Phys. Rev. E*, **78**, 031113, https://doi.org/10.1103/PhysRevE.78.031113.

——, 2014: Unraveling the cause-effect relation between time series. *Phys. Rev. E*, **90**, 052150, https://doi.org/10.1103/PhysRevE.90.052150.

——, 2015: Normalizing the causality between time series. *Phys. Rev. E*, **92**, 022126, https://doi.org/10.1103/PhysRevE.92.022126.

——, 2016: Information flow and causality as rigorous notions ab initio. *Phys. Rev. E*, **94**, 052201, https://doi.org/10.1103/PhysRevE.94.052201.

——, 2021: Normalized multivariate time series causality analysis and causal graph reconstruction. *Entropy*, **23**, 679, https://doi.org/10.3390/e23060679.

——, F. Xu, Y. Rong, R. Zhang, X. Tang, and F. Zhang, 2021: El Niño Modoki can be mostly predicted more than 10 years ahead of time. *Sci. Rep.*, **11**, 17860, https://doi.org/10.1038/s41598-021-97111-y.

——, D. Chen, and R. Zhang, 2023: Quantitative causality, causality-aided discovery, and causal machine learning. *Ocean-Land-Atmos. Res.*, **2**, 0026, https://doi.org/10.34133/olar.0026.

Lloyd, S., 1991: Causality and information flow. *Information Dynamics*, H. Atmanspacher and H. Scheingraber, Eds., Springer, 131–142.

Ma, X., and Coauthors, 2016: Western boundary currents regulated by interaction between ocean eddies and the atmosphere. *Nature*, **535**, 533–537, https://doi.org/10.1038/nature18640.

McPhaden, M. J., and S. P. Hayes, 1991: On the variability of winds, sea surface temperature, and surface layer heat content in the western equatorial Pacific. *J. Geophys. Res.*, **96**, 3331–3342, https://doi.org/10.1029/90JC01726.

Menkes, C. E. R., J. G. Vialard, S. C. Kennan, J.-P. Boulanger, and G. V. Madec, 2006: A modeling study of the impact of tropical instability waves on the heat budget of the eastern equatorial Pacific. *J. Phys. Oceanogr.*, **36**, 847–865, https://doi.org/10.1175/JPO2904.1.

Patrizio, C. R., and D. W. J. Thompson, 2022: Understanding the role of ocean dynamics in midlatitude sea surface temperature variability using a simple stochastic climate model. *J. Climate*, **35**, 3313–3333, https://doi.org/10.1175/JCLI-D-21-0184.1.

Renault, L., M. J. Molemaker, J. C. McWilliams, A. F. Shchepetkin, F. Lemarié, D. Chelton, S. Illig, and A. Hall, 2016: Modulation of wind work by oceanic current interaction with the atmosphere. *J. Phys. Oceanogr.*, **46**, 1685–1704, https://doi.org/10.1175/JPO-D-15-0232.1.

Reynolds, R. W., T. M. Smith, C. Liu, D. B. Chelton, K. S. Casey, and M. G. Schlax, 2007: Daily high-resolution-blended analyses for sea surface temperature. *J. Climate*, **20**, 5473–5496, https://doi.org/10.1175/2007JCLI1824.1.

Seo, H., and Coauthors, 2023: Ocean mesoscale and frontal-scale ocean–atmosphere interactions and influence on large-scale climate: A review. *J. Climate*, **36**, 1981–2013, https://doi.org/10.1175/JCLI-D-21-0982.1.

Shannon, C. E., 1948: A mathematical theory of communication. *Bell Syst. Tech. J.*, **27**, 379–423, https://doi.org/10.1002/j.1538-7305.1948.tb01338.x.

Simmons, A., S. Uppala, D. Dee, and S. Kobayashi, 2006: ERA-interim: New ECMWF reanalysis products from 1989 onwards. *ECMWF Newsletter*, No. 110, ECMWF, Reading, United Kingdom, 25–36.

Small, R. J., and Coauthors, 2008: Air–sea interaction over ocean fronts and eddies. *Dyn. Atmos. Oceans*, **45**, 274–319, https://doi.org/10.1016/j.dynatmoce.2008.01.001.

——, F. O. Bryan, S. P. Bishop, and R. A. Tomas, 2019: Air–sea turbulent heat fluxes in climate models and observational analyses: What drives their variability? *J. Climate*, **32**, 2397–2421, https://doi.org/10.1175/JCLI-D-18-0576.1.

Stips, A., D. Macias, C. Coughlan, E. Garcia-Gorriz, and X. S. Liang, 2016: On the causal structure between CO_2 and global temperature. *Sci. Rep.*, **6**, 21691, https://doi.org/10.1038/srep21691.

Sun, X., and R. Wu, 2022: Spatial scale dependence of the relationship between turbulent surface heat flux and SST. *Climate Dyn.*, **58**, 1127–1145, https://doi.org/10.1007/s00382-021-05957-9.

Sutton, R., and P.-P. Mathieu, 2002: Response of the atmosphere–ocean mixed-layer system to anomalous ocean heat-flux convergence. *Quart. J. Roy. Meteor. Soc.*, **128**, 1259–1275, https://doi.org/10.1256/003590002320373283.

von Storch, J.-S., 2000: Signatures of air–sea interactions in a coupled atmosphere–ocean GCM. *J. Climate*, **13**, 3361–3379, https://doi.org/10.1175/1520-0442(2000)013<3361:SOASII>2.0.CO;2.

Wallace, J. M., C. Smith, and Q. Jiang, 1990: Spatial patterns of atmosphere-ocean interaction in the northern winter. *J. Climate*, **3**, 990–998, https://doi.org/10.1175/1520-0442(1990)003<0990:SPOAOI>2.0.CO;2.

Wu, R., B. P. Kirtman, and K. Pegion, 2006: Local air–sea relationship in observations and model simulations. *J. Climate*, **19**, 4914–4932, https://doi.org/10.1175/JCLI3904.1.

Yang, Y., G. Fu, X. S. Liang, R. H. Weisberg, and Y. Liu, 2023: Causal relations between the loop current penetration and the inflow/outflow conditions inferred with a rigorous quantitative causality analysis. *Deep-Sea Res. II*, **209**, 105298, https://doi.org/10.1016/j.dsr2.2023.105298.

Yi, B., and S. Bose, 2022: Quantum Liang information flow as causation quantifier. *Phys. Rev. Lett.*, **129**, 020501, https://doi.org/10.1103/PhysRevLett.129.020501.